

Article

Effect of Temperature on Luminescence of LiNbO₃ Crystals Single-Doped with Sm³⁺, Tb³⁺, or Dy³⁺ Ions

Radosław Lisiecki *^{id}, Bogusław Macalik, Robert Kowalski, Jarosław Komar^{id}
and Witold Ryba-Romanowski

Division of Optical Spectroscopy, Institute of Low Temperature and Structure Research, Polish Academy of Sciences, Okólna 2, 50-422 Wrocław, Poland; b.macalik@intibs.pl (B.M.); r.kowalski@intibs.pl (R.K.); j.komar@intibs.pl (J.K.); w.ryba-romanowski@intibs.pl (W.R.-R.)

* Correspondence: r.lisiecki@intibs.pl

Received: 8 October 2020; Accepted: 11 November 2020; Published: 13 November 2020



Abstract: Crystals of LiNbO₃ single-doped with Sm³⁺, Tb³⁺, or Dy³⁺ and crystal of LiTaO₃ single-doped with Tb³⁺ were grown by the Czochralski method. Luminescence spectra and decay curves for LiNbO₃ samples containing Sm³⁺ or Dy³⁺ ions were recorded at different temperatures between 295 and 775 K, whereas those for samples containing Tb³⁺ ions were recorded at different temperatures between 10 and 300 K. Optical absorption spectra at different temperatures were recorded within the UV-blue region relevant to optical pumping of the samples. It was found that the effect of temperature on experimental luminescence lifetimes consists of the initial temperature-independent stage followed by a steep decrease with the onset at about 700, 600, and 150 K for Sm³⁺, Dy³⁺, and Tb³⁺ ions, respectively. Additionally, comparison of temperature impact on luminescence properties of LiNbO₃:Tb³⁺ and LiTaO₃:Tb³⁺ crystals has been adequately described. Experimental results were interpreted in terms of temperature-dependent charge transfer (CT) transitions within the modified Temperature—Dependent Charge Transfer phenomenological model (TDCT). Disparity of the onset temperatures and their sequence were explained based on the location of familiar zigzag curves connecting the ground state levels of rare earth ions with respect to the band-gap of the host. It was concluded also that LiNbO₃:Sm³⁺ is suitable as an optical sensor within the 500–750 K temperature region whereas LiNbO₃:Dy³⁺ offers the highest sensitivity at lower temperatures between 300 and 400 K.

Keywords: LiNbO₃; LiTaO₃; oxide crystals; lanthanides; luminescence

1. Introduction

Originally proposed in 1964, LiNbO₃ was soon applied in second harmonic generation, electro-optic modulation, acousto-optic, and piezoelectric device application [1]. Subsequent investigation has revealed that it is promising for holographic recording [2,3], optical parametric oscillation [4,5], waveguide lasers [6,7], or self-frequency doubled lasers [8].

However, despite the long-lasting technological success, some fundamental properties of LiNbO₃ remain rather puzzling. One of encountered difficulties refers to the reliability of its band gap. Numerous reported band gap values, all inferred from optical absorption spectra, range from 3.28 [9] to 4.3 eV [10] with the most frequently cited value of 3.78 eV. This is due mainly to the fact that the LiNbO₃ crystals, suitable for optical application, are fabricated commonly by the Czochralski method from a congruent, lithium deficient melt (Li/Nb = 0.94). Hence, they have a high density of point defects which affect the reliability of the measurement. Even with special care near where stoichiometric crystals have grown, recorded optical absorption spectra still suffered from remaining structural defects. Numerous attempts have been made to determine the band gap from ab initio

calculations. The calculated band gap values depended markedly on the method applied, ranging from 3.47 to 6.53 eV [11]. Authors of a subsequent paper [12] entitled: “Do we know the band gap of lithium niobate?” have reported the calculated band gap value of 4.7 eV and more recently, the calculated band gap value of 4.9 eV has been reported in [13].

Much attention has been paid in the past to the nature of defects in crystal structures of isostructural LiNbO₃ and LiTaO₃ compounds. In the ideal, stoichiometric composition of the cations Nb⁵⁺, Li⁺, and free sites are located sequentially in distorted octahedra of oxygen ions. The distribution of cations among available sites in congruent LiNbO₃ crystals is not easy, however. In the past it has been interpreted in the framework of the Nb-site vacancy model [14]. Later on, it has been concluded that the Nb split models in which the excess of Nb atoms are distributed among the Li and the vacant cation sites cannot be excluded [15]. The same difficulty relates to the location of incorporated luminescent rare earth ions. Investigation of Eu³⁺ sites in LiNbO₃:Eu³⁺ and LiNbO₃:MgO:Eu³⁺ crystals for different Li/Nb molar ratios has led to the conclusion that Eu³⁺ ions substitute the Li⁺ and Nb⁵⁺ ions [16]. The RBS/channeling spectra of Pr³⁺, Ho³⁺, Yb³⁺ ions in LiNbO₃ revealed that they substitute Li⁺ ions but are slightly shifted from the regular Li⁺ position [17]. In a more recent paper dealing with structural and optical properties of powders of LiTaO₃ doped with Eu³⁺ ions the authors have observed that the Eu³⁺ ions substitute preferentially the Ta⁵⁺ ions [18]. Moreover, it was found that this preference increases with increasing Eu³⁺ concentration (an occupation fraction above 60% for Eu³⁺ concentration of 1 at %). In the present work we deal with LiNbO₃ crystal single-doped with Sm³⁺, Tb³⁺, or Dy³⁺ ions characteristic in that the relaxation of their metastable levels consists essentially of radiative transitions in virtually all inorganic hosts.

In fact, spectroscopic features of Sm³⁺-doped crystals and glasses stem from the energy level scheme of Sm³⁺ ions that consist of low-energy multiplets from the ⁷F and ⁷H terms and a higher-energy group of multiplets from quartet terms. The energy difference between the quartet and septet states is large as compared to the phonon energy encountered in inorganic matrices. Therefore, the relaxation of the ⁴G_{5/2} metastable level of Sm³⁺ consists essentially of radiative transitions providing an efficient visible emission. Its spectral distribution within the blue, yellow, and red regions is weakly affected by the change of a host [19–24]. Spectroscopic properties of Tb³⁺-doped hosts stem from the energy level scheme of Tb³⁺ ions involving low-energy multiplets from the ⁷F term and higher-energy multiplets from quintet terms. The metastable 5D₄ level of Tb³⁺ is located higher than the next lower energy ⁷F₀ level by about 14,000 cm⁻¹. Therefore, its relaxation consists essentially of radiative transitions providing an efficient visible emission. Literature concerning spectroscopic features of Tb³⁺ doped luminescent materials is rather rich. The mechanism of the ⁵D₃–⁵D₄ cross-relaxation in Y₃Al₅O₁₂:Tb³⁺ was considered in [25]. Several papers were devoted to preparation and spectroscopic features of terbium-doped garnet crystals [26–29]. Other visible phosphors containing Tb³⁺ ions that have been studied include Y₂LuCaAl₂SiO₁₂:Ln (Ln = Ce³⁺, Eu³⁺, and Tb³⁺) [30], Tb³⁺ doped lithium lead alumino borate glasses [31], Tb³⁺-doped KLu(WO₄)₂ crystal [32], Tb³⁺-doped LiYF₄ [33], Tb³⁺-doped K₃YF₆ [34]. Laser potential and laser performance of Tb³⁺-doped hosts have been considered, too [35]. Spectroscopic properties of Dy³⁺-doped materials stem from the energy level scheme of Dy³⁺ ions that consists of high-energy multiplets from quartet terms well separated from low-energy multiplets belonging to the ⁶H and ⁶F terms. The visible emission of Dy³⁺ results from radiative transitions that originate on the metastable 4F_{9/2} level and terminate on the lower-energy levels ⁶H_J (J = 9/2, 11/2, 13/2, and 15/2). Numerous recent papers have been devoted to Phosphor materials single-doped with Dy³⁺ [36], co-doped with Dy+Eu [37] or triple-doped with Dy+Eu+Tb [38] have been investigated and found promising for novel lighting devices. The potential of Dy³⁺-doped crystals as luminescent temperature sensors has been considered in numerous papers [39–41]. It has been demonstrated that YAG:Dy³⁺ crystal pumped at 447 nm with a GaN laser diode is able to show yellow laser operation with a slope efficiency of 12% [42]. Optical amplification in Dy³⁺-doped Gd₂SiO₅, Lu₂SiO₅, and YAl₃(BO₃)₄ single crystals has been observed [43] as well. Intention of the present work is to get a closer insight into temperature-dependent processes which are relevant for

excited state relaxation of incorporated rare earth ions and to assess the impact of these processes on the potential of system studied for luminescence temperature sensing.

2. Materials and Methods

Single-doped crystals of LiNbO_3 containing nominally 0.65 wt% (1.2×10^{20} ions/cm³) of Sm^{3+} , 2.80 wt% (4.8×10^{20} ions/cm³) of Tb^{3+} , or 1.94 wt% (3.3×10^{20} ions/cm³) of Dy^{3+} were grown by the Czochralski method from the congruent melt ($\text{Li/Nb} = 0.945$). By the same method a 3 wt% Tb^{3+} -doped LiTaO_3 crystal was grown creating thereby a reference material to help understand the $\text{LiNbO}_3:\text{Tb}^{3+}$ luminescence. The Czochralski growth of LiNbO_3 and LiTaO_3 crystals has been well known for decades and is described in detail elsewhere, e.g., in [44]. Concentrations given above stem from the trade-off between the intention to achieve required excitation efficiency, on one hand, and to prevent the excessive distortion of the host structure, on the other hand. A Varian 5E UV-VIS-NIR spectrophotometer with instrumental spectral bandwidths of 0.5 nm was employed to record optical absorption spectra in the UV-blue spectral region. To record excitation spectra and luminescence spectra a FLS980 fluorescence spectrophotometer from Edinburg Instruments equipped with a 450 W xenon lamp as an excitation source and a Hamamatsu 928 PMT detector was used. For these measurements, the samples were excited with unpolarized light propagating parallel to the optical axis of the crystal and the luminescence was observed perpendicular to the optical axis of the crystal. Recorded spectra were corrected for the sensitivity and wavelength of the experimental set-up. To record decay curves of luminescence an experimental set-up consisting of a tunable optical parametric oscillator (OPO) pumped by a third harmonic of a Nd:YAG laser, a double grating monochromator with a 1000 mm focal length, a photomultiplier, and a Tektronix MDO 4054B-3 Mixed Domain Oscilloscope was used. For spectroscopic measurement at low temperature the samples were placed in an Oxford Model CF 1204 continuous flow liquid helium cryostat equipped with a temperature controller. A chamber furnace was used for measurements at higher temperature within 295–800 K. The temperature of samples was detected by a copper-constant thermocouple with measurement error less than 1.5 K and controlled by a proportional-integral-derivative (PID) Omron E5CK controller.

3. Results

When interpreting our experimental data, we refer to energy level schemes for Sm^{3+} , Tb^{3+} , and Dy^{3+} ions gathered in Figure 1. The energy levels within respective $4f^5$, $4f^6$, and $4f^7$ configurations are labeled by symbols $^{2S+1}L_J$ of corresponding multiplets.

It can be seen that there is a correspondence between term structures for Sm^{3+} and Dy^{3+} ions in agreement with the principle of electrons and holes in the $4f^n$ configurations. Actually, each multiplet of rare earth ions incorporated in the crystal host is split by the crystal field into crystal field components. In depth analysis of the crystal field splitting of multiplets for Sm^{3+} and Dy^{3+} ions in LiNbO_3 has been performed based on low temperature absorption and emission spectra and reported in [45,46], respectively. These results were used to construct corresponding energy level schemes shown in Figure 1. To our knowledge the information concerning the crystal field splitting of Tb^{3+} in LiNbO_3 is not available. Therefore, we include in Figure 1 the data for Tb^{3+} in GAGG garnet reported in [29]. It should be noticed here that the agreement between theoretical and experimental crystal field splitting inferred from low temperature spectra of rare earth ions in LiNbO_3 is poor owing to multi-site location of incorporated ions combined with a strong inhomogeneous line broadening of their optical spectra. Other consequences result from a strongly defective congruent composition of the hosts crystal. The LiNbO_3 forms crystals that belong to trigonal/rhombohedral system, $R3c$ space group, hence they are optically uniaxial. Incorporated rare earth ions enter sites with the C_3 local symmetry in the stoichiometric composition but in congruent LiNbO_3 they are located in several nonequivalent sites with strongly dissimilar local symmetries. As a consequence, the anisotropy of their transition intensities is no longer consistent with theoretical predictions preventing thereby the reliable interpretation of polarized optical spectra, as observed in [45,46]. To avoid the difficulties mentioned

above and remembering that effect of temperature on integrated luminescence intensity is independent of polarization of optical spectra we infer our results from unpolarized luminescence spectra.

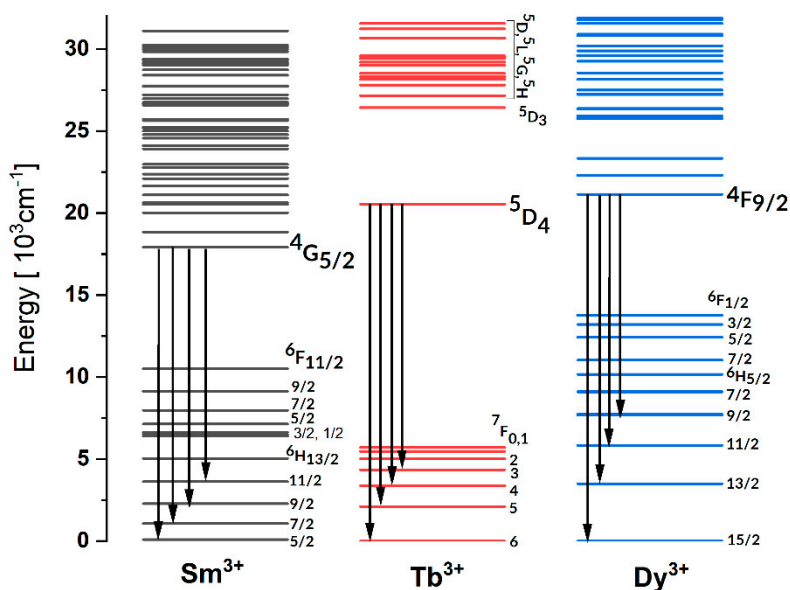


Figure 1. Energy level schemes for Sm^{3+} , Tb^{3+} , and Dy^{3+} . Vertical downward arrows indicate transitions involved.

In the limit of low doping level, the population of an excited multiplet decays by competing radiative transitions and nonradiative multiphonon relaxation consisting of simultaneous emission of several phonons. The contribution of the latter process is commonly assessed from the phenomenological energy gap law which relates the rate of multiphonon relaxation to the order of the process defined as the ratio of energy separation between the excited level in question and a next lower level to the cut-off phonon energy available in the host. It follows from the Raman spectra analysis of LiNbO_3 and LiTaO_3 crystals that the highest energy stretching vibrations Nb-O are around 610 cm^{-1} (597 cm^{-1} for Ta-O) [47]. Thus, Sm^{3+} , Tb^{3+} , and Dy^{3+} ions in LiNbO_3 have single metastable levels able to relax radiatively without multiphonon contribution providing thereby intense luminescence. Downward arrows in Figure 1 indicate radiative transitions observed in the visible region.

3.1. Effect of Temperature on Luminescence of Sm^{3+} and Dy^{3+} in LiNbO_3

On the right side of Figure 2 we compare survey room temperature luminescence spectra of Sm^{3+} and Dy^{3+} ions in LiNbO_3 recorded within the 450–800 nm spectral region. Sm^{3+} luminescence was excited at 402 nm. Its luminescence spectrum consists of bands located at about 567, 600, 646, and 708 nm related to transitions between the metastable $4\text{G}_{5/2}$ level and 6H_J ($J = 5/2, 7/2, 9/2, 11/2$) terminal levels, respectively. Very weak contribution of the $4\text{G}_{5/2} \rightarrow 6\text{H}_{13/2}$ transition can be discerned around 800 nm. It should be noticed here that there are other transitions from the $4\text{G}_{5/2}$ level, namely to the multiplets of the 6F term and the $4\text{G}_{5/2} \rightarrow 6\text{H}_{15/2}$ transition, all of them located in the near IR. The contribution of these transitions to luminescence spectra of samarium ions in crystals and glasses is marginal and therefore is commonly neglected. Dy^{3+} luminescence shown in Figure 2 was excited at 356 nm. Its luminescence spectrum consists of bands located at about 486, 580, 665, and 754 nm related to transition between the metastable $4\text{F}_{9/2}$ level and 6H_J ($J = 15/2, 13/2, 11/2, \text{ and } 9/2$) terminal levels, respectively. Remaining transitions from the metastable $4\text{F}_{9/2}$ level are located in the IR and terminate on multiplets of the 6F term and on the $6\text{H}_{7/2}$ and $6\text{H}_{5/2}$ multiplets. Their contribution to dysprosium luminescence is very weak, as for samarium luminescence.

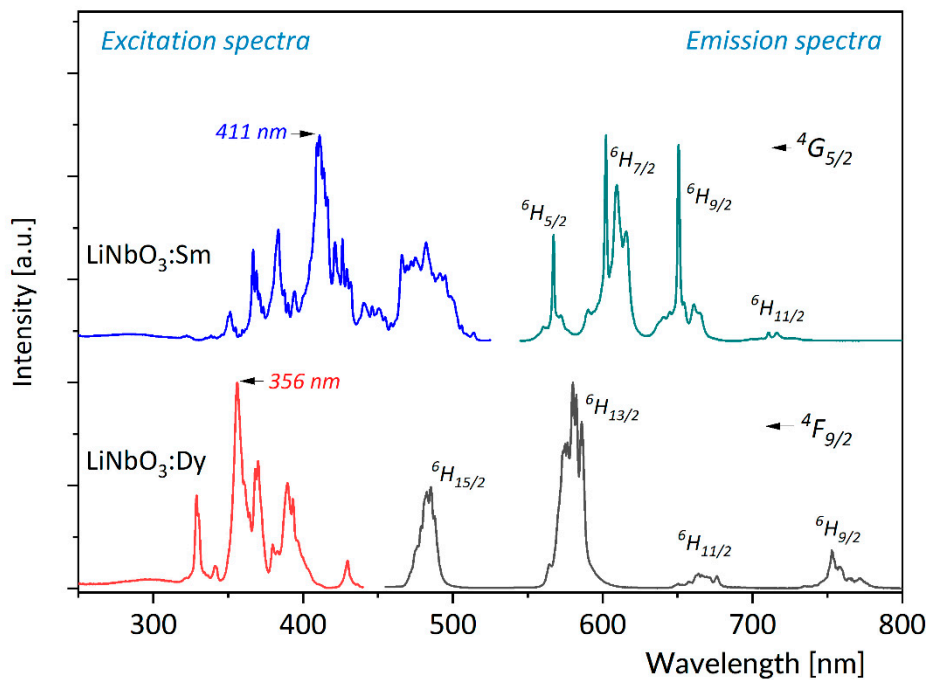


Figure 2. Survey, room temperature luminescence spectra of Sm^{3+} and Dy^{3+} ions in LiNbO_3 recorded within the 450–800 nm spectral region (**right**) and excitation spectra of Sm^{3+} and Dy^{3+} luminescence in LiNbO_3 , monitored at 611 and 573 nm, respectively (**left**).

On the left side of Figure 2 we compare excitation spectra of Sm^{3+} luminescence and Dy^{3+} luminescence in LiNbO_3 , monitored at 611 and at 573 nm, respectively. Excitation spectra for the two ions show very complex structure of band components corresponding to closely spaced transitions from the ground states to high energy multiplets derived from the ^4F , ^4G , ^4H , ^4I , ^4K , ^4L , ^4M quartet and the ^6P sextet terms. It should be noticed here that despite a rich spectrum, the intensity of absorption in this spectral region is very low because spin forbidden sextet-quartet transitions are involved. It can be seen that the highest energy bands contributing to excitation spectra in Figure 2 are located around 411 and 356 nm although the energy level schemes of two ions contain levels at higher energy. Rather curiously, the wavelength 335 nm correspond to 3.7 eV, a value of the most frequently cited energy gap for LiNbO_3 . In view of theoretical calculations mentioned above in Section 1 the short wavelength limit of the excitation spectra may not be due to the fundamental UV absorption edge of LiNbO_3 . It may result also from an absorption of color centers, likely to exist in the matrix and/or transitions between the ground states of incorporated rare earth ions and trapped exciton states, as proposed for $\text{LiTaO}_3:\text{Pr}$ system [47,48].

Figure 3 compares luminescence spectra of Sm^{3+} in LiNbO_3 recorded at different temperatures between 295 K and 775 nm. Excitation was at 402 nm. It can be seen that with increasing temperature the contribution of narrow band components to the spectrum vanishes gradually, the bands become smoother and their intensities diminish. To assess the effect of temperature on the overall Sm^{3+} luminescence the spectra recorded at different temperatures were integrated numerically within the 450–750 nm region. Results of this assessment presented in the inset on the right side of Figure 3 reveal the adverse thermally induced quenching of Sm^{3+} emission. The inset on the left side of Figure 3 shows spectra for the high energy part of the spectrum between 460 and 550 nm, where the luminescence grows monotonously.

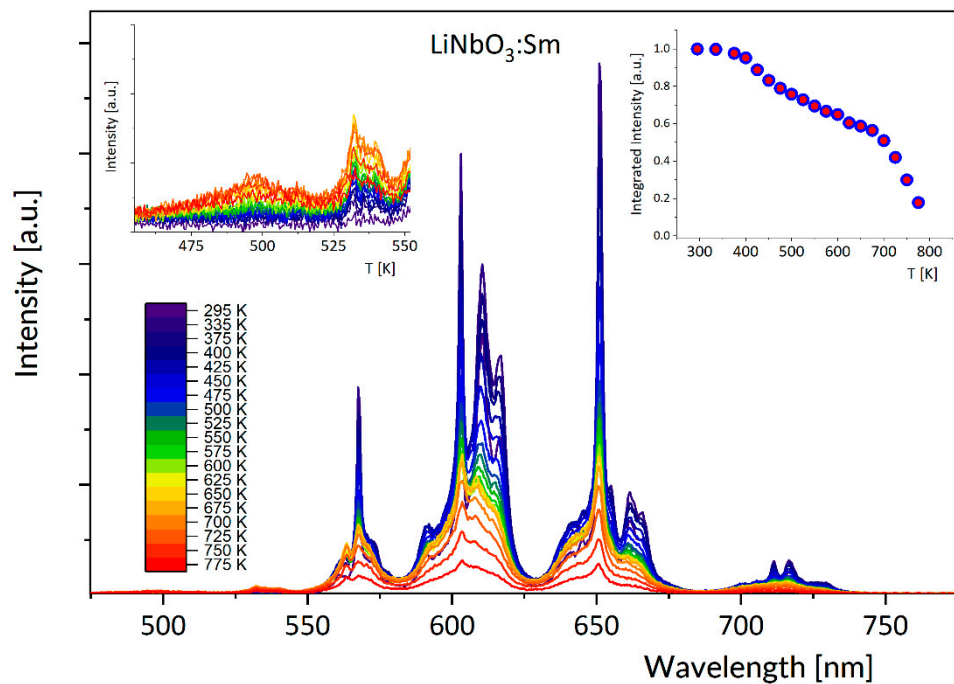


Figure 3. Luminescence spectra of Sm^{3+} in LiNbO_3 recorded at different temperatures between 295 and 775 K. Excitation was at 402 nm. Left inset: Magnified spectra of the high energy part of the spectrum between 460 and 550 nm. Right inset: Integrated luminescence intensity plotted versus temperature.

Examination of luminescence spectra of Dy^{3+} in LiNbO_3 excited at 356 nm and recorded at different temperatures between 295 and 723 K reveal similar thermal effect.

Namely, the contribution of narrow band components to the spectrum vanishes gradually, the bands become more smooth and their intensities diminish, except for the high energy part of the spectrum between 440 and 500 nm, where the luminescence grows steadily. For the sake of brevity, the spectra shown in Figure 4 are restricted to the short wavelength parts encompassing bands within the 440–550 nm region. The Dy^{3+} luminescence intensities determined by a numerical integration of spectra within the 440–750 nm region are plotted versus temperature in the inset on the right. The inset on the left side shows the onset of steep rise of the sample absorption in the UV region observed at several different temperatures. Examination of plots in insets on the right side of Figures 3 and 4 reveals a thermally enhanced quenching of both the Sm^{3+} and Dy^{3+} luminescence in LiNbO_3 . This phenomenon may be due to a thermally induced decrease of absorption efficiency in the optical pump region and/or to thermally enhanced increase of nonradiative relaxation rates of the metastable $4G_{5/2}$ and $4F_{9/2}$ levels of Sm^{3+} and Dy^{3+} , respectively. The contribution of these quenching factors can be assessed based on examination of Figure 5.

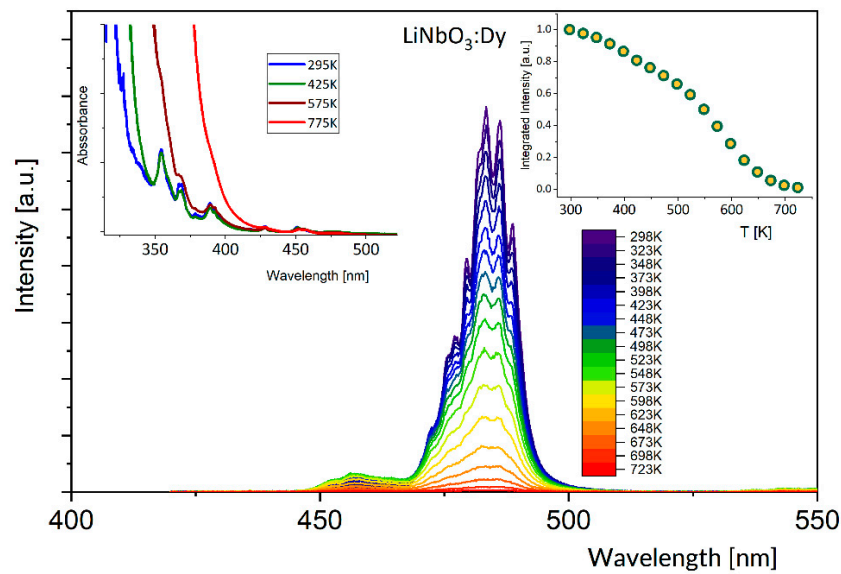


Figure 4. Luminescence spectra between 440 and 500 nm for Dy^{3+} in LiNbO_3 recorded at different temperatures between 295 and 723 K. Excitation was at 356 nm. Left inset: The onset of steep rise of the sample absorption in the UV region observed at several different temperatures. Right inset: Integrated luminescence intensity plotted versus temperature.

Table 1. Spectral parameters governing the temperature dependence of ${}^4\text{G}_{5/2}$ (Sm^{3+}) and ${}^4\text{F}_{9/2}$ (Dy^{3+}) lifetimes in LiNbO_3 within the framework of the TDCTmodel.

	$\text{LiNbO}_3:\text{Sm}$	$\text{LiNbO}_3:\text{Dy}$
W_{nr} (1/s)	855	508
E_a (cm^{-1})	16,159	14,795
α (cm^{-1}/K)	23.3	26.1
$\hbar\omega$ (cm^{-1})	672	680
W_r (1/s)	1540	5164

Points in this figure show the temperature dependence of the ${}^4\text{G}_{5/2}$ and ${}^4\text{F}_{9/2}$ experimental lifetimes determined experimentally from respective exponential luminescence decay curves. It can be seen that initially, i.e., up to about 700 K for Sm^{3+} and up to about 600 K for Dy^{3+} , the luminescence lifetimes do not depend on temperature implying that the contribution of the latter factor can be neglected. Therefore, we attribute the decrease of integrated luminescence intensity observed in this initial temperature region to thermally induced increase of a broad-band absorption that affects adversely the efficiency of optical pumping. In fact, the onset of this absorption shifts towards longer wavelengths when the temperature increases, as shown in the inset on the left side of Figure 4. Further increase of the temperature brings about a very steep decrease of the lifetime values. At 775 K, the highest temperature provided by our experimental setup, the Dy^{3+} lifetime is close to zero whereas the Sm^{3+} lifetime attains about 70% of its value at room temperature.

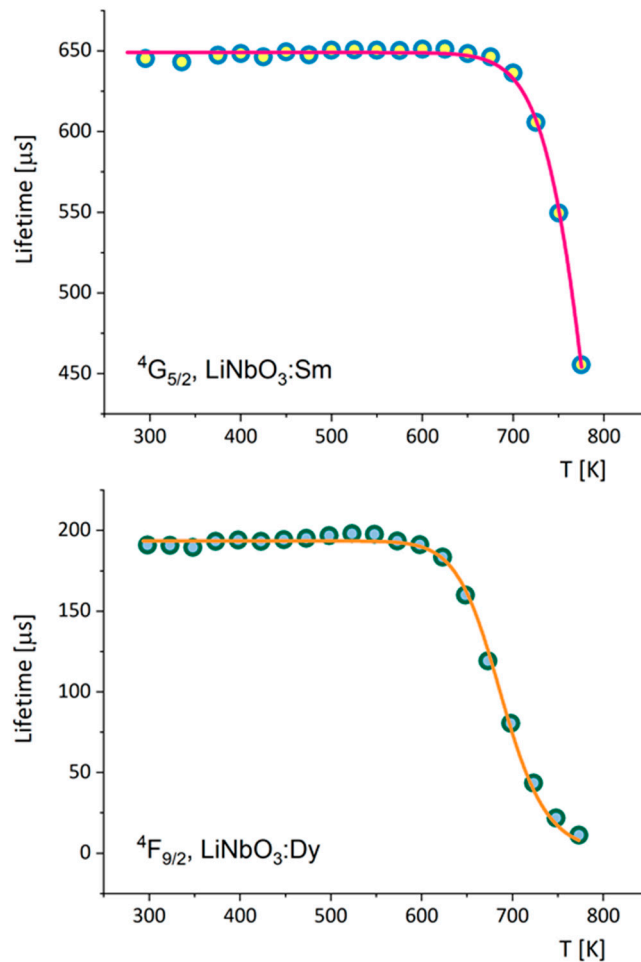


Figure 5. Temperature dependence of ${}^4G_{5/2}$ (Sm^{3+}) and ${}^4F_{9/2}$ (Dy^{3+}) lifetimes in LiNbO₃. Points indicate experimental data. Solid lines represent theoretical temperature dependence determined from Equation (2) with parameters gathered in Table 1.

To interpret the effect of temperature on the ${}^4G_{5/2}$ and ${}^4F_{9/2}$ lifetimes, shown in Figure 5 one should remember that the measured luminescence lifetime τ_{exp} of an excited level of rare earth ion.

$$\tau_{exp} = 1/[W_r + W_{nr}] \quad (1)$$

where W_r is the temperature independent radiative decay rate and W_{nr} denotes the rate of nonradiative decay affected by the temperature. Following the interpretation of data acquired for LiTaO₃:Pr³⁺ [47] and recent generalization on spectroscopy of Pr³⁺ in niobate-titanates [48] we interpret the steep decrease of Sm³⁺ and Dy³⁺ lifetimes in terms of temperature-dependent charge transfer (CT) transitions within the modified model (TDCT) proposed by Nikolic et al. [40]. According to the TDCT model the rate $W_{nr}(T)$ of nonradiative charge transfer transitions

$$W_{nr}(T) = W_{nr}(0) \times \left(\frac{1}{T^{*\frac{1}{2}}} \right) \times \exp[(-E_a + \alpha T)/k_B T^*] \quad (2)$$

where T denotes the temperature, $W_{nr}(0)$ denotes the rate of the process at 0 K, E_a is the energy barrier to be crossed by phonons, k_B is the Boltzmann constant. The factor αT represents the thermally induced change of the energy E_a assumed to be linear with the slope α .

The factor

$$T^* = \left(\frac{\hbar\omega}{2k_B} \right) \times \coth(\hbar\omega/2k_B T) \quad (3)$$

included to the above relation accounts for the non-Arrhenius nature of the excitation energy flow through CT states [49]. The $\hbar\omega$ denotes the energy of the host phonons involved. Solid lines in Figure 5 represent theoretical temperature dependence of Sm^{3+} and Dy^{3+} lifetimes determined from Equation (2) with parameters gathered in Table 1. It can be seen that their agreement with experimental data points is reasonable.

In the following we focus our attention to temperature dependent changes of luminescence bands related to transitions that terminate on the ${}^6\text{H}_{5/2}$ ground state of Sm^{3+} and the ${}^6\text{H}_{15/2}$ ground state of Dy^{3+} . It follows from Figures 3 and 4 that there are contributions of luminescence that grow monotonously with increasing temperature at the expense of the ${}^4\text{G}_{5/2} \rightarrow {}^6\text{H}_{5/2}$ and ${}^4\text{F}_{9/2} \rightarrow {}^6\text{H}_{15/2}$ bands located at slightly longer wavelengths. Examination of low temperature absorption spectra reported in the past [45,46] reveals that these growing contributions in the Sm^{3+} spectrum is due to transitions from thermally populated ${}^4\text{F}_{3/2}$ level and that in the Dy^{3+} spectrum from thermally populated ${}^4\text{I}_{15/2}$ level. These levels are located, respectively, above the ${}^4\text{G}_{5/2}$ and ${}^4\text{F}_{9/2}$ metastable levels by about 1000 cm^{-1} only and therefore their populations are governed by the Boltzmann statistics. Accordingly, a thermally induced change of fluorescence intensity ratio (FIR) between the ${}^4\text{F}_{3/2} \rightarrow {}^6\text{H}_{5/2}$ and ${}^4\text{G}_{5/2} \rightarrow {}^6\text{H}_{5/2}$ emission bands for Sm^{3+} and between the ${}^4\text{I}_{15/2} \rightarrow {}^6\text{H}_{15/2}$ and ${}^4\text{F}_{9/2} \rightarrow {}^6\text{H}_{15/2}$ emission bands for Dy^{3+} can be applied as the temperature sensing parameter. It is known that the luminescence intensities are proportional to the population of involved energy levels and FIR of two thermally coupled levels can be defined by following equation [39]:

$$\text{FIR} = \frac{I_{4\text{I}_{15/2}}}{I_{4\text{F}_{9/2}}} = B \exp\left(-\frac{\Delta E}{kT}\right) \quad (4)$$

where B is temperature independent constant, ΔE is the energy gap between the two thermally coupled levels, and k is the Boltzmann constant. Plots of FIR versus temperature for $\text{LiNbO}_3:\text{Sm}^{3+}$ and $\text{LiNbO}_3:\text{Dy}^{3+}$ are compared in Figure 6.

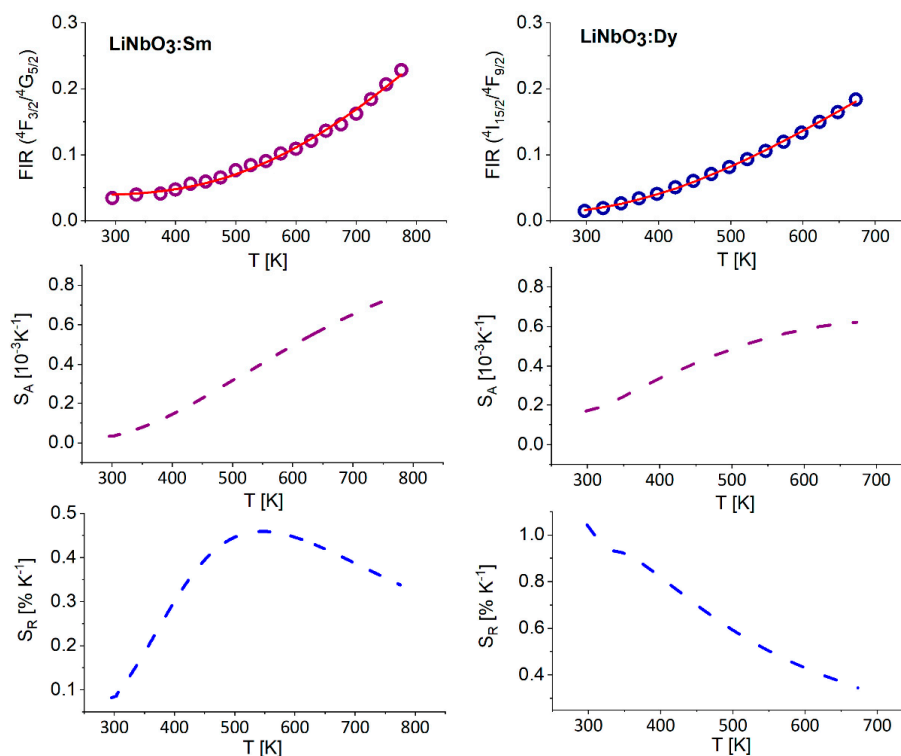


Figure 6. Plots of FIR versus temperature for $\text{LiNbO}_3:\text{Sm}^{3+}$ and $\text{LiNbO}_3:\text{Dy}^{3+}$ (upper graphs) and plots of S_A and S_R parameters versus temperature for $\text{LiNbO}_3:\text{Sm}^{3+}$ (left) and $\text{LiNbO}_3:\text{Dy}^{3+}$ (right).

Points indicate experimental data determined from spectra in Figures 3 and 4 and the solid lines represent fits of Equation (4) with $\Delta E = 1139 \text{ cm}^{-1}$ (for Sm^{3+}) and $\Delta E = 1146 \text{ cm}^{-1}$ (for Dy^{3+}).

Optical thermometer may be quantitatively characterized with absolute and relative thermal sensitivity. The former parameter reveals the absolute FIR change with temperature variation and is expressed as:

$$S_A = \frac{dFIR}{dT} = FIR \frac{\Delta E}{kT^2} \quad (5)$$

To reliably compare the thermometers quality, relative sensitivity is usually used because this parameter determines normalized change of FIR with temperature variation and is defined as [39]:

$$S_R = \frac{1}{FIR} \frac{dFIR}{dT} \cdot 100\% = \frac{\Delta E}{kT^2} \cdot 100\% \quad (6)$$

Figure 6 compares also plots of S_A and S_R parameters versus temperature for $\text{LiNbO}_3:\text{Sm}^{3+}$ (left) and $\text{LiNbO}_3:\text{Dy}^{3+}$ (right). Examination of the S_R plots indicates that the $\text{LiNbO}_3:\text{Sm}^{3+}$ is mostly suitable for the optical sensor within the 500–750 K temperature region whereas $\text{LiNbO}_3:\text{Dy}^{3+}$ offers the highest sensitivity at lower temperatures between 300 and 400 K. However, the most significant shortcoming of these optical sensors resides in that their luminescence is quenched at temperatures markedly lower as compared to other hosts doped with Sm^{3+} and Dy^{3+} .

3.2. Effect of Temperature on Luminescence of Tb^{3+} in LiNbO_3 and LiTaO_3

Points in Figure 7 show the temperature dependence of the $^5\text{D}_4$ lifetime determined experimentally from luminescence decay curves. Unlike $\text{LiNbO}_3:\text{Sm}^{3+}$ and $\text{LiNbO}_3:\text{Dy}^{3+}$ systems the $\text{LiNbO}_3:\text{Tb}^{3+}$ shows luminescence below ambient temperature only but still the dependence of its lifetime on the temperature consists of the initial part weakly affected by the temperature up to about 130 K and of subsequent steep decrease. For a comparison the experimental $^5\text{D}_4$ lifetime for $\text{LiTaO}_3:\text{Tb}^{3+}$ plotted versus temperature also in Figure 7 is nearly constant at temperatures up to about 480 K and next decreases steeply. Solid lines in Figure 7 represent theoretical temperature dependence of the $^5\text{D}_4$ lifetime for $\text{LiNbO}_3:\text{Tb}^{3+}$ and $\text{LiTaO}_3:\text{Tb}^{3+}$ determined from Equation (2) with parameters gathered in Table 2. It is worth noticing here that LiNbO_3 and LiTaO_3 compounds form isostructural crystals characterized by very similar physicochemical properties. Incorporated luminescent rare earth ions are located in sites with the same symmetry in these hosts. They interact with lattice phonons having similar energy distribution with nearly the same cut-off energy corresponding to Nb-O or Ta-O stretching vibrations [47]. Thus, rather small disparity between spectral features of Tb^{3+} in the two hosts can be supposed. Indeed, the survey luminescence spectra of $\text{LiNbO}_3:\text{Tb}^{3+}$ and of $\text{LiTaO}_3:\text{Tb}^{3+}$ compared in Figure 8 corroborate this supposition.

3.3. Discussion

Results presented above imply that the location of the metastable $^5\text{D}_4$ level of Tb^{3+} with respect to the bottom of conduction band of the host is a factor that governs the luminescence quenching. Obviously, for a given band-gap the energy difference between the bottom of the conduction band and the metastable $^5\text{D}_4$ level results from the energy difference between the Tb^{3+} ground state and the top of the valence band. The latter difference can be assessed based on generalizations proposed by Dorenbos et al. and by Dorenbos in a series of published papers, e.g., [50,51]. In particular, the ground state of Tb^{3+} located previously 0.7–1.0 eV higher above the valence band than that of Pr^{3+} has been adjusted based on new experimental data showing that these locations are at about the same energy [51]. The band-gap of LiTaO_3 has been determined in the past to be 4.59 eV, a value corresponding to the UV absorption edge located at 271 nm [52]. The available information on band-gap of LiNbO_3 is not reliable in view of the controversy mentioned above in Section 1 but the disparity of band-gap values for the two hosts is likely to be small. In any case, we suppose that peculiarities of luminescence quenching in $\text{LiNbO}_3:\text{Tb}^{3+}$ and $\text{LiTaO}_3:\text{Tb}^{3+}$ are not governed by the band-gaps but stem from the fact

that in LiTaO₃ the ground state of Tb³⁺ is located lower, i.e., closer to the valence band than in LiNbO₃. It follows from the zigzag curves connecting the ground state levels of rare earth ions [50,51] that among rare earth ions considered here the ground state of Tb³⁺ is located at the highest energy, that of Dy³⁺ is located markedly lower and that of Sm³⁺ at the lowest energy. In principle, the energy difference between the top of the valence band and the ground state level of the rare earth ion in question can be determined provided the energy of the charge transfer (denoted also IVCT = intervalence charge transfer) transition and the band-gap of the host are known. Unfortunately, we were not able to obtain these data from our measurement. Figure 2 shows that the IVCT transitions do not contribute to excitation spectra of Sm³⁺ and Dy³⁺ luminescence. Additionally, the IVCT transition does not contribute to the excitation spectrum of Tb³⁺ luminescence in LiNbO₃. In [53] the IVCT transition energy of about 3.4 eV for Pr³⁺ in LiNbO₃ has been mentioned. Assuming that the band-gap of LiNbO₃ equals to 3.8 eV we locate the ground state of Pr³⁺ at about 0.4 eV above the top of the valence band. With this assumption and supposing that the ground states of Pr³⁺ and Tb³⁺ are located at the same energy we locate the ⁵D₄ metastable level of Tb³⁺ at around 0.86 eV below the conduction band. This calculation is rather speculative and the reliability of the ⁵D₄ location is not certain. However, it is worth noticing that it locates the ground states of Sm³⁺ and Dy³⁺ below the top of the valence band accounting for the absence of IVCT band in excitation spectra of their luminescence. The onset of the steep decrease of luminescence lifetime, related with the IVCT, occurs at about 700, 600, and 150 K for Sm³⁺, Dy³⁺, and Tb³⁺ ions in LiNbO₃, respectively. The ⁴G_{5/2} metastable level of Sm³⁺ is located at about 17,600 cm⁻¹, i.e., about 2.18 eV above the ground state level. The ⁴F_{9/2} metastable level of Dy³⁺ is located at about 21,100 cm⁻¹ i.e., about 2.61 eV above the ground state level. These values, combined with those inferred from the zigzag curve predict that the energy barrier to be crossed by phonons would be higher, hence the onset temperature would be also higher for Sm³⁺, in agreement with experimental data. The ⁵D₄ metastable level of Tb³⁺ is located at about 2.55 eV above the ground state level, a value slightly smaller than that for Dy³⁺. However, this location combined with a relatively large energy inferred from the zigzag curve results in markedly smaller energy barrier hence the lower onset temperature.

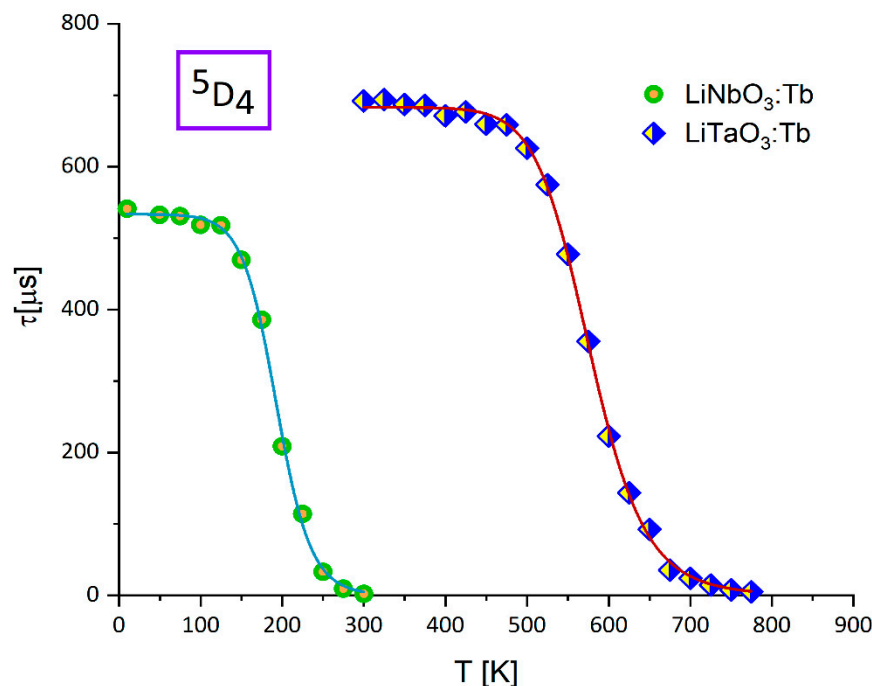


Figure 7. Temperature dependence of ⁵D₄ (Tb³⁺) lifetimes in LiNbO₃ and LiTaO₃. Points indicate experimental data. Solid lines represent theoretical temperature dependence determined from Equation (1) with parameters gathered in Table 2.

Table 2. Spectral parameters governing the temperature dependence of 5D_4 (Tb^{3+}) lifetimes in $LiNbO_3$ and $LiTaO_3$ within the framework of the TDCT model.

	$LiNbO_3:Tb$	$LiTaO_3:Tb$
W_{nr} (1/s)	1064	807
E_a (cm^{-1})	1984	8128
α (cm^{-1}/K)	17.1	17.6
$\hbar\omega$ (cm^{-1})	693	778
W_r (1/s)	1874	1464

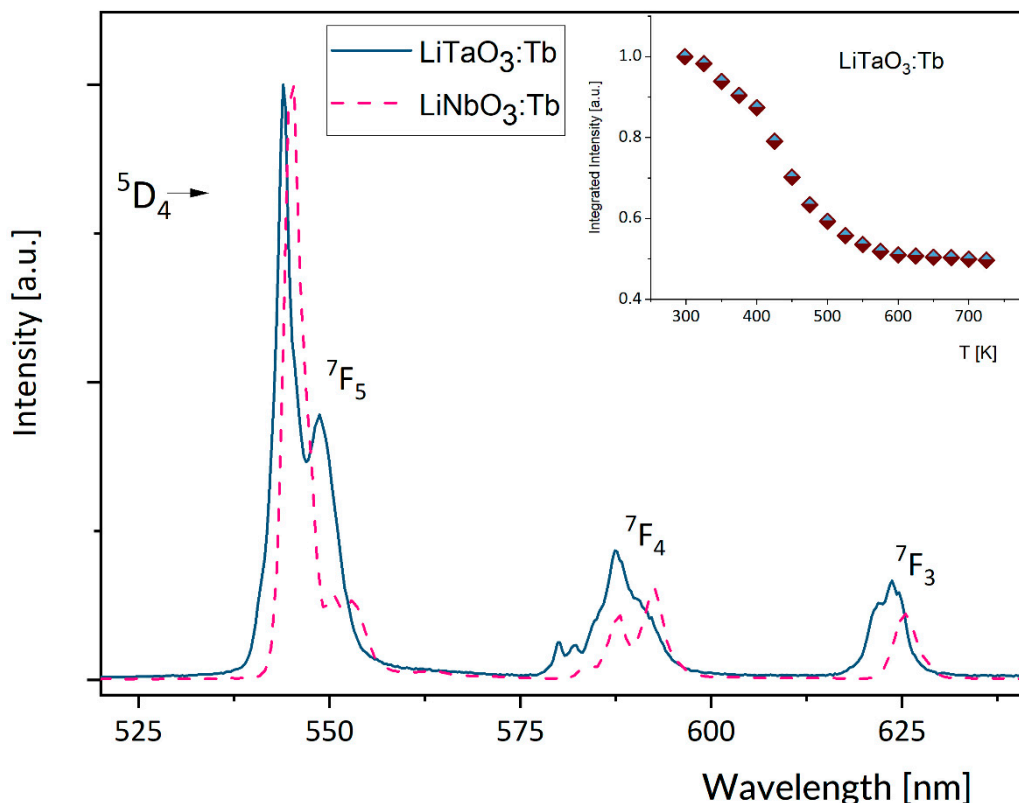


Figure 8. Comparison of the survey luminescence spectrum of $LiNbO_3:Tb^{3+}$ recorded at 10 K to survey luminescence spectrum of $LiTaO_3:Tb^{3+}$ recorded at 300 K. Inset shows effect of temperature on integrated emission intensity of $LiTaO_3:Tb^{3+}$.

4. Conclusions

The effect of temperature on experimental luminescence lifetimes consists of the initial temperature-independent stage followed by a steep decrease with the onset at about 700, 600, and 150 K for Sm^{3+} , Dy^{3+} , and Tb^{3+} ions, respectively. Experimental results were interpreted in terms of temperature-dependent charge transfer (CT) transitions within the modified phenomenological model TDCT. Disparity of the onset temperatures and their sequence were explained based on the location of familiar zigzag curves connecting the ground state levels of rare earth ions with respect to the band-gap of the host. It was concluded also that $LiNbO_3:Sm^{3+}$ is suitable as an optical sensor within the 500–750 K temperature region whereas $LiNbO_3:Dy^{3+}$ offers the highest sensitivity at lower temperatures between 300 and 400 K.

Author Contributions: Conceptualization, R.L. and W.R.-R.; methodology, R.L., B.M., R.K. and J.K.; software, J.K.; validation, R.L. and W.R.-R.; formal analysis, R.L., B.M., R.K. and J.K.; investigation, R.L., B.M., R.K. and J.K.; resources, W.R.-R.; data curation, R.L., B.M., R.K. and J.K.; writing—original draft preparation, R.L. and W.R.-R.; writing—review and editing, R.L. and W.R.-R.; visualization, R.L., B.M., R.K. and J.K.; supervision, R.L. and W.R.-R.; project administration, R.L. and W.R.-R.; funding acquisition, W.R.-R.; All authors have read and agreed to the published version of the manuscript.

Funding: The work was financially supported within the statutory funds of the Institute of Low Temperature and Structure Research, Polish Academy of Sciences in Wrocław.

Conflicts of Interest: The authors declare no conflict of interest.

References

1. Boyd, G.D.; Miller, R.C.; Nassau, K.; Bond, W.L.; Savage, A. LiNbO₃: An efficient phase matchable nonlinear optical material. *Appl. Phys. Lett.* **1964**, *5*, 234. [[CrossRef](#)]
2. Lee, M.; Takedawa, S.; Furukawa, Y.; Kitamura, K.; Hatano, H.; Tanaka, S. Nonvolatile two-color holographic recoding in Tb-doped LiNbO₃. *Appl. Phys. Lett.* **2000**, *76*, 1653–1655. [[CrossRef](#)]
3. Adibi, A.; Buse, K.; Psaltis, D. Two-center holographic recording. *J. Opt. Soc. Am. B* **2001**, *18*, 584–601. [[CrossRef](#)]
4. Myers, L.E.; Eckhardt, R.C.; Fejer, M.M.; Byer, R.L.; Bosenberg, W.R.; Pierce, J.W. Quasi-phase-matched optical parametric oscillations in bulk periodically poled LiNbO₃. *J. Opt. Soc. Am.* **1995**, *B12*, 2102–2116. [[CrossRef](#)]
5. Ross, G.W.; Pollnau, M.; Smith, P.G.R.; Clarkson, W.A.; Britton, P.E.; Hanna, D.C. Generation of high-power blue light in periodically poled LiNbO₃. *Opt. Lett.* **1998**, *23*, 171–173. [[CrossRef](#)]
6. Lallier, E.; Pachole, J.P.; Papuchon, M.; Micheli, M.; Li, M.J.; He, Q.; Ostrovsky, D.B.; Grezes-Besset, C.; Pelletier, E. Nd:MgO:LiNbO₃ waveguide laser and amplifier. *Opt. Lett.* **1990**, *15*, 682–684. [[CrossRef](#)]
7. Amin, J.; Aust, J.A.; Veasey, D.L.; Sanfard, N.A. Dual wavelength 980 nm pumped Er/Yb-codoped waveguide laser in Ti:LiNbO₃. *Electron. Lett.* **1998**, *34*, 456–458. [[CrossRef](#)]
8. Li, R.; Wang, C.J.; Liang, X.; Peng, K.; Xu, G. CW Nd:Mg:LiNbO₃ self-frequency-doubling laser at room temperature. *IEEE J. Quantum Electron.* **1993**, *29*, 2419–2420. [[CrossRef](#)]
9. Jiangou, Z.; Shipin, Z.; Dingquan, X.; Xiu, W.; Guanfeng, X. Optical absorption properties of doped lithium niobate crystals. *J. Phys. Condens. Matter.* **1992**, *4*, 2977. [[CrossRef](#)]
10. Kase, S.; Ohi, K. Optical absorption and interband Faraday rotation in LiTaO₃ and LiNbO₃. *Ferroelectrics* **1974**, *8*, 419. [[CrossRef](#)]
11. Schmidt, W.G.; Albrecht, M.; Wippermann, S.; Blankenburg, S.; Rauls, E.; Fuchs, F.; Rodl, C.; Furthmüller, J.; Hermann, A. LiNbO₃ ground- and excited-state properties from first-principles calculations. *Phys. Rev. B* **2006**, *77*, 035106. [[CrossRef](#)]
12. Thierfelder, C.; Sanna, S.; Schindlmayr, A.; Schmidt, W.G. Do we know the band gap of lithium niobate? *Phys. Stat. Solidi C* **2010**, *7*, 362–365. [[CrossRef](#)]
13. Mamoun, S.; Merad, A.E.; Guilbert, L. Energy band gap and optical properties of lithium niobate from ab initio calculations. *Comp. Mater. Sci.* **2013**, *79*, 125–131. [[CrossRef](#)]
14. Abrahams, S.C.; Marsh, P. Defect structure dependence on composition in lithium niobate. *Acta Cryst. B* **1986**, *42*, 61. [[CrossRef](#)]
15. Iyi, N.; Kitamura, K.; Izumi, F.; Yamamoto, J.K.; Hayashi, K.; Asano, H.; Kimura, J. Comparative study of defect structures in lithium niobate with different compositions. *J. Solid State Chem.* **1992**, *101*, 340. [[CrossRef](#)]
16. Zotov, N.; Boysen, H.; Frey, F.; Metzger, T.; Born, E. Cation substitution models of congruent LiNbO₃ investigated by X-ray and neutron powder diffraction. *J. Phys. Chem. Solids* **1994**, *55*, 145–152. [[CrossRef](#)]
17. Lorenzo, A.; Jaffrezic, H.; Roux, B.; Boulon, G.; Garcia-Sole, J. Lattice location of rare earth ions in LiNbO₃. *Appl. Phys. Lett.* **1995**, *67*, 3735. [[CrossRef](#)]
18. Gasparotto, G.; Cebim, M.A.; Goes, M.S.; Lima, S.A.M.; Davolos, M.R.; Varela, J.A.; Paiva-Santos, C.O.; Zaghete, M.A. Correlation between the spectroscopic and structural properties with the occupation of the Eu³⁺ sites in powdered Eu³⁺-doped LiTaO₃ prepared by the Pechini method. *J. Appl. Phys.* **2009**, *106*, 063509. [[CrossRef](#)]
19. Shu, S.; Wang, Y.; Ke, Y.; Deng, B.; Liu, R.; Song, Q.; Wang, J.; Yu, R. NaCaTiTaO₆:Sm³⁺: A novel orange-red-emitting tantalate phosphor with excellent thermal stability and high color purity for white LEDs. *J. Alloy. Compd.* **2020**, *848*, 156359. [[CrossRef](#)]

20. Su, K.; Zhang, Q.; Yang, X.; Ma, B. Crystal structure and luminescence properties of thermally stable Sm³⁺-doped Sr₉In(PO₄)₇ orange-red phosphor. *J. Phys. D Appl. Phys.* **2020**, *53*, 385101. [[CrossRef](#)]
21. Zhang, L.; Che, J.; Ma, Y.; Wang, J.; Kang, R.; Deng, B.; Yu, R.; Geng, H. Luminescent and thermal properties of novel orange-red emitting Ca₂MgTeO₆:Sm³⁺ phosphors for white LED's. *J. Lumin.* **2020**, *225*, 117374. [[CrossRef](#)]
22. Kovács, L.; Kocsor, L.; Tichy-Rács, É.; Lengyel, K.; Bencs, L.; Corradi, G. Hydroxyl ion probing transition metal dopants occupying Nb sites in stoichiometric LiNbO₃. *Opt. Mater. Express* **2019**, *9*, 4506–4516. [[CrossRef](#)]
23. Mandula, G.; Kis, Z.; Kovacs, L.; Szaller, Z.; Krampf, A. Site-selective measurement of relaxation properties at 980 nm in Er³⁺-doped congruent and stoichiometric lithium niobite crystals. *Appl. Phys. B* **2016**, *122*, 72. [[CrossRef](#)]
24. Kis, Z.; Mandula, G.; Lengyel, K.; Hajdara, I.; Kovacs, L.; Imlau, M. Homogeneous linewidth measurements of Yb³⁺ ions in congruent and stoichiometric lithium niobate crystals. *Opt. Mater.* **2014**, *37*, 845–853. [[CrossRef](#)]
25. Robbins, D.J.; Cockayne, B.; Lent, B.; Glasper, J.L. The mechanism of ⁵D₃–⁵D₄ cross-relaxation in Y₃Al₅O₁₂:Tb³⁺. *Solid State Commun.* **1976**, *20*, 673–676. [[CrossRef](#)]
26. Park, J.Y.; Jung, H.C.; Raju, S.R.; Moon, B.K.; Jeong, J.H.; Kim, J.H. Solvothermal synthesis and luminescence properties of Tb³⁺-doped gadolinium aluminum garnet. *J. Lumin.* **2010**, *130*, 478–482. [[CrossRef](#)]
27. Praveena, R.; Shim, J.J.; Cai, P.; Seo, H.J.; Chung, W.; Kwon, T.H.; Jayasankar, C.K.; Haritha, P.; Venkatramu, V. Luminescence properties of Lu₃Al₅O₁₂:Tb³⁺ nano-garnet. *J. Korean Phys. Soc.* **2014**, *64*, 1859–1865. [[CrossRef](#)]
28. Teng, X.; Wang, W.; Cao, Z.; Li, J.; Duan, G.; Liu, Z. The development of new phosphors 3f Tb³⁺/Eu³⁺ co-doped Gd₃Al₅O₁₂ with tunable emission. *Opt. Mater. (Amst.)* **2017**, *69*, 175–180. [[CrossRef](#)]
29. Solarz, P.; Głowacki, M.; Lisiecki, R.; Sobczyk, M.; Komar, J.; Macalik, B.; Ryba-Romanowski, W. Impact of temperature on excitation, emission and cross-relaxation processes of terbium ions in GGAG single crystal. *J. Alloy. Compd.* **2019**, *789*, 409–415. [[CrossRef](#)]
30. Hakeem, D.A.; Pi, J.W.; Kim, S.W.; Park, K. New Y₂LuCaAl₂SiO₁₂:Ln (Ln = Ce³⁺, Eu³⁺, and Tb³⁺) phosphors for white LED applications. *Inorg. Chem. Front.* **2018**, *5*, 1336–1345. [[CrossRef](#)]
31. Deopa, N.; Rao, A.S. Spectroscopic studies of single near ultraviolet pumped Tb³⁺ doped Lithium Lead Alumino Borate glasses for green lasers and tricolour w-LEDs. *J. Lumin.* **2018**, *194*, 56–63. [[CrossRef](#)]
32. Loiko, P.; Volokitina, A.; Mateos, X.; Dunina, E.; Kornienko, A.; Vilejshikova, E.; Aguiló, M.; Díaz, F. Spectroscopy of Tb³⁺ ions in monoclinic KLu(WO₄)₂ crystal application of an intermediate configuration interaction theory. *Opt. Mater.* **2018**, *78*, 495–501. [[CrossRef](#)]
33. Liu, G.K.; Carnall, W.T.; Jones, R.P.; Cone, R.L.; Huang, J. Electronic energy level structure of Tb³⁺ in LiYF₄. *J. Alloy. Compd.* **1994**, *207–208*, 69–73. [[CrossRef](#)]
34. Gusowski, M.A.; Ryba-Romanowski, W. Unusual behavior of Tb³⁺ in K₃YF₆ green-emitting phosphor. *Opt. Lett.* **2008**, *33*, 1786–1788. [[CrossRef](#)] [[PubMed](#)]
35. Metz, P.W.; Marzahl, D.T.; Huber, G.; Kränkel, C. Performance and wavelength tuning of green emitting terbium lasers. *Opt. Express* **2017**, *25*, 5716. [[CrossRef](#)]
36. Rajendra, H.J.; Pandurangappa, C.; Monika, D.L. Luminescence properties of dysprosium doped YVO₄ phosphor. *J. Rare Earths* **2018**, *36*, 1245–1249. [[CrossRef](#)]
37. Liu, Y.; Liu, G.; Wang, J.; Dong, X.; Yu, W. Multicolor photoluminescence and energy transfer properties of dysprosium and europium-doped Gd₂O₃ phosphors. *J. Alloy. Compd.* **2015**, *649*, 96–103. [[CrossRef](#)]
38. Rimbach, A.C.; Steudel, F.; Ahrens, B.; Schweizer, S. Tb³⁺, Eu³⁺, and Dy³⁺ doped lithium borate and lithium aluminoborate glass: Glass properties and photoluminescence quantum efficiency. *J. Non Cryst. Solids* **2018**, *499*, 380–386. [[CrossRef](#)]
39. Perera, S.S.; Rabuffetti, F.A. Dysprosium-activated scheelite-type oxides as thermosensitive phosphors. *J. Mater. Chem. C* **2019**, *7*, 7601. [[CrossRef](#)]
40. Nikolić, M.G.; Jovanović, D.J.; Dramićanin, M.D. Temperature dependence of emission and lifetime in Eu³⁺- and Dy³⁺-doped GdVO₄. *Appl. Opt.* **2013**, *52*, 1716–1724. [[CrossRef](#)]
41. Hertle, E.; Chepyga, L.; Batentschuk, M.; Will, S.; Zigan, L. Temperature-dependent luminescence characteristics of Dy³⁺ doped in various crystalline hosts. *J. Lumin.* **2018**, *204*, 64–74. [[CrossRef](#)]
42. Bowman, S.R.; O'Connor, S.; Condon, N.J. Diode pumped yellow dysprosium lasers. *Opt. Express* **2012**, *20*, 12906–12911. [[CrossRef](#)] [[PubMed](#)]

43. Haro-González, P.; Martín, L.L.; Martín, I.R.; Berkowski, M.; Ryba-Romanowski, W. Optical amplification properties of Dy³⁺-doped Gd₂SiO₅, Lu₂SiO₅ and YAl₃(BO₃)₄ single crystals. *Appl. Phys. B Lasers Opt.* **2011**, *103*, 597–602. [[CrossRef](#)]
44. Repelin, Y.; Husson, E.; Proust, F.B.C. Raman spectroscopy of lithium niobate and lithium tantalite. Force field calculations. *J. Phys. Chem. Solids* **1999**, *60*, 819–825. [[CrossRef](#)]
45. Dominiak-Dzik, G. Sm³⁺-doped LiNbO₃ crystal, optical properties and emission cross-sections. *J. Alloy. Compd.* **2005**, *391*, 26–32. [[CrossRef](#)]
46. Dominiak-Dzik, G.; Ryba-Romanowski, W.; Palatnikov, M.N.; Sidorov, N.V.; Kalinnikov, V.T. Dysprosium-doped LiNbO₃ crystal. Optical properties and effect of temperature on fluorescence dynamics. *J. Mol. Struct.* **2004**, *704*, 139–144. [[CrossRef](#)]
47. Gryk, W.; Dyl, D.; Ryba-Romanowski, W.; Grinberg, M. Spectral properties of LiTaO₃:Pr³⁺ under high hydrostatic pressure. *J. Phys. Condens. Matter* **2005**, *17*, 5381–5395. [[CrossRef](#)]
48. Boutinaud, P. Rationalization of the Pr³⁺-to-transition metal charge transfer model: Application to the luminescence of Pr³⁺ in titano-nobates. *J. Lumin.* **2019**, *214*, 116557. [[CrossRef](#)]
49. Englman, R.; Jortner, J. The energy gap law for radiationless transitions in large molecules. *J. Mol. Phys.* **1970**, *18*, 145. [[CrossRef](#)]
50. Dorenbos, P.; Krumpel, A.H.; Boutinaud, E.v.P.; Bettinelli, M.; Cavalli, E. Lanthanide level location in transition metal complex compounds. *Opt. Mater.* **2010**, *32*, 1681–1685. [[CrossRef](#)]
51. Dorenbos, P. Charge transfer bands in optical materials and related defect level location. *Opt. Mater.* **2017**, *69*, 8–22. [[CrossRef](#)]
52. Nikl, M.; Morlotti, R.; Magro, C.; Bracco, R. Emission and storage properties of LiTaO₃:Tb³⁺ phosphor. *J. Appl. Phys.* **1996**, *79*, 2853–2856. [[CrossRef](#)]
53. Boutinaud, P.; Bettinelli, M.; Diaz, F. Intervalence charge transfer in Pr³⁺-and Tb³⁺-doped double tungstate crystals KRE(WO₄)₂ (RE = Y, Gd, Yb, Lu). *Opt. Mater.* **2010**, *32*, 1659–1663. [[CrossRef](#)]

Publisher's Note: MDPI stays neutral with regard to jurisdictional claims in published maps and institutional affiliations.



© 2020 by the authors. Licensee MDPI, Basel, Switzerland. This article is an open access article distributed under the terms and conditions of the Creative Commons Attribution (CC BY) license (<http://creativecommons.org/licenses/by/4.0/>).